

Spin-Orbit Coupled Degenerate Fermi Gases

Pengjun Wang*,¹ Zeng-Qiang Yu^{†,2} Zhengkun Fu,¹ Jiao Miao,²
Lianghui Huang,¹ Shijie Chai,¹ Hui Zhai,^{2,‡} and Jing Zhang^{1,§}

¹*State Key Laboratory of Quantum Optics and Quantum Optics Devices,
Institute of Opto-Electronics, Shanxi University, Taiyuan 030006, P.R.China*
²*Institute for Advanced Study, Tsinghua University, Beijing, 100084, P.R.China*

Spin-orbit coupling plays an increasingly important role in the modern condensed matter physics. For instance, it gives birth to topological insulators and topological superconductors. Quantum simulation of spin-orbit coupling using ultracold Fermi gases will offer opportunities to study these new phenomena in a more controllable setting. Here we report the first experimental study of a spin-orbit coupled Fermi gas. We observe spin dephasing in spin dynamics and momentum distribution asymmetry in the equilibrium state as hallmarks of spin-orbit coupling. We also observe evidences of Lifshitz transition where the topology of Fermi surfaces change. This serves as an important first step toward finding Majorana fermions in this system.

In the past decade, quantum simulations with ultracold atoms have investigated many fascinating quantum phenomena in a highly controllable and tunable way. Studies of ultracold Fermi gases with resonant interaction have shed lights on understanding strongly interacting fermion systems in nature, including neutron stars and quark-gluon plasma; simulating Fermi Hubbard model with optical lattices helps to understand the physical mechanism of unconventional high- T_c superconductors. However, until very recently, an important interaction has not been explored in cold atom systems, that is, the spin-orbit (SO) coupling. Recently using two-photon Raman process, SO coupled Bose-Einstein condensate has been realized in the laboratory [1], which gives rise to new quantum phases such as stripe superfluid [2, 3]. In real materials, SO coupling plays an important role in many physical systems over a wide range of energy scale, from determining the nuclear structure inside a nuclei, and the electronic structure inside an atom, to giving birth to topological insulators in solid state materials [4, 5]. Since all these systems are fermionic, from the viewpoint of quantum simulation it is desirable to experimentally realize SO coupled degenerate Fermi gases. The physical effects of SO coupling in a degenerate Fermi gas are quite different from those in a Bose system. In this work we report the first experimental study of a SO coupled degenerate Fermi gas. Evidences of SO coupling have been obtained from both the Raman induced quantum spin dynamics and the spin-resolved momentum distribution. With SO coupling, we also observe evidences for Lifshitz transition where the Fermi surface changes its topology as the density of fermion increases. This progress will enable us to study stronger pairing and higher T_c enhanced by SO coupling in resonant interacting Fermi gases [6–9] and topological insulator and topological superfluid in a more flexible setup [10, 11] in the near future.

In ultracold atom systems, SO coupling is generated through atom-light interaction induced artificial gauge fields, and therefore it has two advantages. First, both the strength and the configuration of SO coupling are

tunable via controlling the atom-light coupling; Secondly, the coefficient of SO coupling is naturally on the same order of the inverse of laser wavelength, and in a gaseous system it gives rise to a coupling strength as strong as the Fermi energy. In this regime SO coupling dramatically changes the density-of-state at Fermi energy and the topology of Fermi surface, which gives rise to many intriguing phenomena in many-body systems [6–12], while such a regime is not easy to access in conventional solid state materials.

In our experiment, a degenerate Fermi gas of 2×10^6 ^{40}K atoms in the lowest hyperfine state $|F = 9/2, m_F = 9/2\rangle$ state is first prepared in an optical dipole trap. The optical dipole trap is composed of two horizontal crossed beams of 1064 nm at 90° along the $\hat{x} \pm \hat{y}$ direction overlapped at the focus, as shown in Fig. 1(a). The temperature of the Fermi gas is about 0.3-0.4 T_F (T_F the Fermi temperature) when the trap frequency reaches $2\pi \times (116, 116, 164)$ Hz along $(\hat{x}, \hat{y}, \hat{z})$ direction (see *Methods* for details). We can change the trap frequency adiabatically to achieve different fermion density. A pair of Helmholtz coils (green ones in Fig. 1(a)) provides a homogeneous bias magnetic field along \hat{y} (quantization axis), which is precisely controlled by a carefully designed scheme described in Ref. [13] to reduce the magnetic field drift and the magnetic noise.

The method we used to generate SO coupling is the same as reported by the NIST group for the ^{87}Rb Bose condensate [1]. In the ^{40}K system, two spin-1/2 states are chosen as two magnetic sublevels $|\uparrow\rangle = |F = 9/2, m_F = 9/2\rangle$ and $|\downarrow\rangle = |F = 9/2, m_F = 7/2\rangle$ of the $F = 9/2$ hyperfine level. They are coupled by a pair of Raman beams with coupling strength Ω . Two Raman lasers with the wavelength $\lambda = 773$ nm and the frequency difference ω counter-propagate along \hat{x} axis and are linearly polarized along \hat{y} and \hat{z} directions, respectively, corresponding to π and σ polarization relative to quantization axis \hat{y} (as shown in Fig. 1(a)). The recoil momentum $k_r = k_0 \sin(\theta/2)$, and recoil energy $E_r = k_r^2/2m = h \times 8.34$ kHz are taken as natural momentum and energy units,

where $k_0 = 2\hbar\pi/\lambda$ and $\theta = 180^\circ$ is the angle between two Raman beams. A Zeeman shift $\omega_Z/2\pi = 10.4$ MHz between these two magnetic sublevels is produced by the homogeneous bias magnetic field at 31 G. When the Raman coupling is at resonance (at $\omega/2\pi = 10.4$ MHz and two-photon Raman detuning $\delta = \hbar(\omega_Z - \omega) \approx 0$), the detuning between $|F = 9/2, m_F = 7/2\rangle$ and other magnetic sublevels like $|F = 9/2, m_F = 5/2\rangle$ is about $h \times 170$ kHz, which is one order of magnitude larger than the Fermi energy. Thus we can safely disregard other levels and treat this system as a spin-1/2 system. Same as in the boson experiment, this scheme generates an effective single particle Hamiltonian as [1]

$$\mathcal{H} = \begin{pmatrix} \frac{1}{2m}(\mathbf{p} - k_r \hat{\mathbf{e}}_x)^2 - \frac{\delta}{2} & \\ \frac{\Omega}{2} & \frac{1}{2m}(\mathbf{p} + k_r \hat{\mathbf{e}}_x)^2 + \frac{\delta}{2} \end{pmatrix} \quad (1)$$

Here, \mathbf{p} denotes the quasi-momentum of atoms, which relates to the real momentum \mathbf{k} as $\mathbf{k} = \mathbf{p} \mp k_r \hat{\mathbf{e}}_x$ with \mp for spin-up and down, respectively. This Hamiltonian can be interpreted as an equal weight combination of Rashba-type and Dresselhaus-type SO coupling [1]. Finally, before time-of-flight measurement, the Raman beams, optical dipole trap and the homogeneous bias magnetic field are turned off abruptly at the same time, and a magnetic field gradient along \hat{y} direction provided by Ioffe coil is turned on. Two spin states are separated along \hat{y} direction during the time-of-flight due to the Stern-Gerlach effect, and imaging of atoms along \hat{z} direction after 12 ms expansion gives the momentum distribution for each spin component.

The main part of this paper is to study manifestation SO coupling in a Fermi gas system. We first study the Rabi oscillation between the two spin states induced by the Raman coupling. This experiment, on one hand, measures the coupling strength Ω ; and on the other hand, clearly manifests different effect of SO coupling compared to boson system. All atoms are initially prepared in the $|\uparrow\rangle$ state. The homogeneous bias magnetic field is ramped to a certain value so that $\delta = -4E_r$, that is, the $\mathbf{k} = 0$ state of $|\uparrow\rangle$ component is at resonance with $\mathbf{k} = 2k_r \hat{\mathbf{e}}_x$ state of $|\downarrow\rangle$ component, as shown in Fig. 1(b). Then we apply a Raman pulse to the system, and measure the spin population for different duration time of the Raman pulse. Similar experiment in boson system yields an undamped and completely periodic oscillation, which can be well described by a sinusoidal function with frequency Ω [14]. This is because for bosons, macroscopic number of atoms occupy the resonant $\mathbf{k} = 0$ mode, and therefore there is a single Rabi frequency determined by the Raman coupling only. While for fermions, due to the Pauli exclusion principle, atoms occupy different momentum states. Precisely due to the effect of SO coupling, the coupling between the two spin states and the resulting energy splitting are momentum dependent, and atoms in different momentum states oscillate with different frequencies (as shown explicitly in Eq. (2) later). Hence,

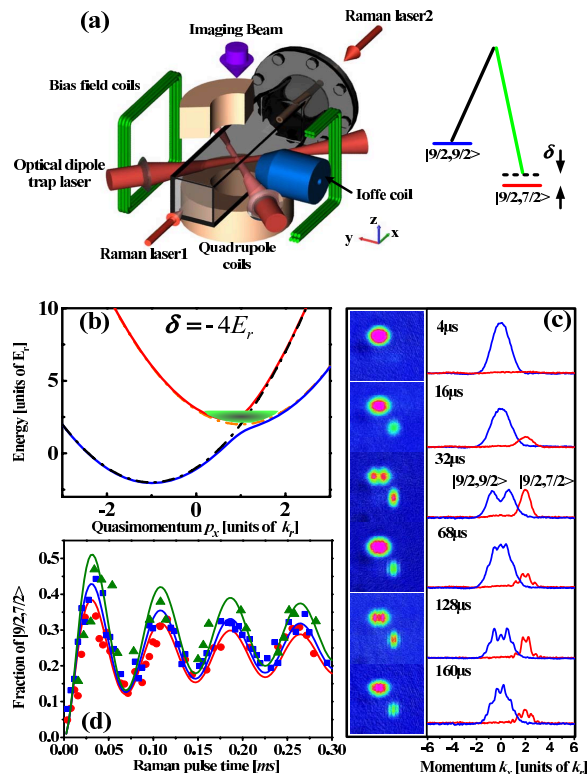


FIG. 1: Experimental setup and Raman-induced quantum spin dynamics: (a) Schematic of experimental setup and the Raman coupling of two hyperfine levels of ^{40}K . (b) The energy dispersion with $\delta = -4E_r$. The system is initially prepared with all atoms in $|9/2, 9/2\rangle$ state. (c) The population in $|9/2, 7/2\rangle$ as a function of duration time of Raman pulse. $k_F = 1.9k_r$ and $T/T_F = 0.30$ for red circles, $k_F = 1.35k_r$ and $T/T_F = 0.35$ for blue squares, $k_F = 1.1k_r$ and $T/T_F = 0.29$ for green triangles. The solid lines are theory curves with $\Omega = 1.52E_r$. (d) Time-of-flight image (left) and integrated time-of-flight image (integrated along \hat{y}) at different duration time for $|\uparrow\rangle$ (blue) and $|\downarrow\rangle$ (red). The parameters are the same as blue ones in (c)

dephasing naturally occurs and the oscillation will be inevitably damped after several oscillation periods. This process is very similar to the spin dynamics of a spin polarized current ejected into a semiconductor. For semiconductor spintronics, one would like to have a polarized spin current, however, because different electron has different velocity and thus their spins precess in different way, the current will be unpolarized. Such spin dynamics has been extensively studied during recent decades [15]. In our case, we can observe momentum-resolved spin dynamics with Stern-Gerlach technique and therefore we can clearly reveal this physical process. In the Fig. 1(c), we show the momentum distribution for both spin components at several different moments. One can see the multiple-peaks feature in momentum distribution in Fig. 1(d), which clearly shows the out-of-phase oscillation for different momentum states.

Unlike bosons, the Raman coupling Ω cannot be read out directly from the period of oscillation. In fact, the frequency depends on both atoms density and temperature, and it is generally smaller than Ω due to the effect of averaging over different momentum states. To determine the value of Ω from the measurements, we fix Raman coupling and vary atoms density by changing the total number of fermions or the trapping frequency, and we obtain several different oscillation curves, as shown in Fig. 1(d). Then we fit them to the theory with a single fitting parameter Ω . Theoretically, for a non-interacting system, the population of $|\downarrow\rangle$ component is given by

$$n_{\downarrow}(\mathbf{k} + 2k_r \hat{\mathbf{e}}_x, \mathbf{r}, t) = n_{\uparrow}(\mathbf{k}, \mathbf{r}, 0) \frac{1}{1 + \left(\frac{2k_x k_r}{\Omega m}\right)^2} \times \sin^2 \sqrt{(k_x k_r / m)^2 + \Omega^2 / 4} t, \quad (2)$$

where t is the duration time of Raman pulse, $n_{\uparrow}(\mathbf{k}, \mathbf{r}, 0)$ is the equilibrium distribution of the initial state in local density approximation, and temperature of initial cloud is determined by fitting the time-of-flight image to momentum distribution of free fermions in a harmonic trap. From Eq. (2) one can see that the momentum distribution along \hat{x} direction of $|\downarrow\rangle$ component is always symmetric respect to $2k_r$ at any time, and the experimental data is indeed the case, as shown in Fig. 1(c). The theoretical expectation of the total population in $|\downarrow\rangle$ component is given by $N_{\downarrow}(t) = \int d^3\mathbf{k} d^3\mathbf{r} n_{\downarrow}(\mathbf{k}, \mathbf{r}, t)$, and in Fig. 1(d), one can see there is an excellent agreement between the experiment data and theory, from which we determine $\Omega = 1.52(5)E_r$. Since our current experiment is performed in the weakly interacting regime with s -wave scattering length $a_s = 169a_0$, we have verified that the interaction effect is negligible (see *Method* for details).

Next, we focus on the case with $\delta = 0$, and study the momentum distribution in the equilibrium state. We first transfer half of ^{40}K atoms from $|\downarrow\rangle$ to $|\uparrow\rangle$ using radio frequency sweep within 100 ms. Then the Raman coupling strength is ramped up adiabatically in 100 ms from zero to its final value and the system is held for another 50 ms before time-of-flight measurement. We have also varied the holding time and find the momentum distribution does not change, and thus we conclude that the system has reached equilibrium in the presence of SO coupling. Since SO coupling breaks spatial reflectional symmetry ($x \rightarrow -x$ and $k_x \rightarrow -k_x$), the momentum distribution for each spin component will be asymmetric, i.e. $n_{\sigma}(\mathbf{k}) \neq n_{\sigma}(-\mathbf{k})$, with $\sigma = \uparrow, \downarrow$; While on the other hand, when $\delta = 0$ the system still preserves time-reversal symmetry, which requires $n_{\uparrow}(\mathbf{k}) = n_{\downarrow}(-\mathbf{k})$. The asymmetry can be clearly seen in the spin-resolved time-of-flight images and integrated distributions displayed in Fig. 2(a) and (b), where the fermion density is relatively low. While it becomes less significant when the fermion density becomes higher, as shown in Fig. 2(c), because the strength of SO coupling is relatively weaker com-

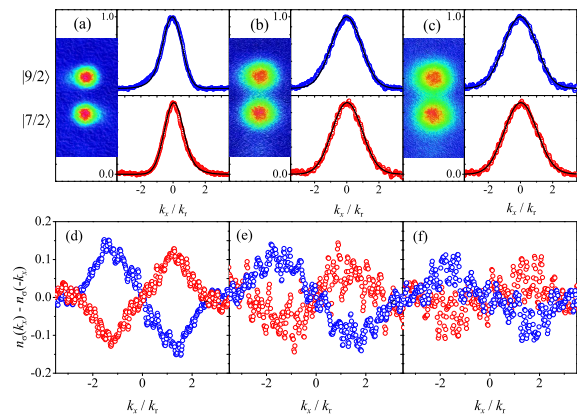


FIG. 2: Momentum distribution asymmetry as a hallmark of SO coupling: (a-c) time-of-flight measurement of momentum distribution for both $|\uparrow\rangle$ (blue) and $|\downarrow\rangle$ (red). Solid lines are theory curves. (a) $k_F = 0.9k_r$ and $T/T_F = 0.8$ (b) $k_F = 1.6k_r$ and $T/T_F = 0.63$; (c) $k_F = 1.8k_r$ and $T/T_F = 0.57$. (d-f): plot of integrated momentum distribution $n_{\sigma}(\mathbf{k}) - n_{\sigma}(-\mathbf{k})$ for the case of (a-c).

pared to the Fermi energy. In Fig. 2(a-c) the integrated momentum distribution is fitted by the theoretical calculation to determine the temperature and the chemical potential at the center of the trap. (See *Method* for detail). We find that the Raman lasers indeed cause additional heating to the cloud. Nevertheless, the temperature we find is within the range of $0.5 - 0.8T_F$ [16], which is still below degenerate temperature. In Fig. 2(d-f), we also show $n_{\sigma}(k_x) - n_{\sigma}(-k_x)$ to reveal the distribution asymmetry more clearly. These are smoking gun evidences of a degenerate Fermi gas with SO coupling.

With SO coupling, the single particle spectra of Eq. 1 are dramatically changed from two parabolic dispersions into two helicity branches as shown in the inset of Fig. 3(a). Here, two different branches are eigenstates of “helicity” \hat{s} and the “helicity” operator describes whether spin $\boldsymbol{\sigma}_{\mathbf{p}}$ is parallel or anti-parallel to the “effective Zeeman field” $\mathbf{h}_{\mathbf{p}} = (-\Omega, 0, k_r p_x / m + \delta)$ at each momentum, i.e. $\hat{s} = \boldsymbol{\sigma}_{\mathbf{p}} \cdot \mathbf{h}_{\mathbf{p}} / |\boldsymbol{\sigma}_{\mathbf{p}} \cdot \mathbf{h}_{\mathbf{p}}|$. $s = 1$ for the upper branch and $s = -1$ for the lower branch. The topology of Fermi surface exhibits two transitions as the atoms density varies. At sufficient low density, it contains two disjointed Fermi surfaces with $s = -1$, and they gradually merge into a single Fermi surface as the density increases to n_{c1} . Finally a new small Fermi surface appears at the center of large Fermi surface when density further increases and fermions begin to occupy $s = 1$ helicity branch at n_{c2} . A theoretical ground state phase diagram for the uniform system is shown in Fig. 3(a), and an illustration of the Fermi surfaces at different density are shown in Fig. 3(b). Across the phase boundaries, the system experiences Lifshitz transitions as density increases [17], which is a unique property in a Fermi gas due to Pauli

principle. At sufficiently low temperature, the derivative of the thermodynamic quantities like the compressibility will exhibit singularity in the critical regime around the transition point.

Rigorously speaking Lifshitz transition only exists at zero temperature and at finite temperature it becomes a crossover. However, we can still obtain several consistent features that supports the existence of such a transition at zero temperature. We fix the Raman coupling and vary the atoms density at the center of the trap by controlling total fermion number or trap frequency, as indicated by the red arrow in Fig. 3(a). The quasi-momentum distribution in the helicity bases can be obtained from a transformation of momentum distribution in spin bases as follows (See *Method* for the definition of $u_{\mathbf{p}}$ and $v_{\mathbf{p}}$):

$$n_{+}(\mathbf{p}) = \frac{u_{\mathbf{p}}^2 n_{\uparrow}(\mathbf{p} - \hbar k_{\text{r}} \hat{\mathbf{e}}_x) - v_{\mathbf{p}}^2 n_{\downarrow}(\mathbf{p} + \hbar k_{\text{r}} \hat{\mathbf{e}}_x)}{u_{\mathbf{p}}^2 - v_{\mathbf{p}}^2} \quad (3)$$

$$n_{-}(\mathbf{p}) = \frac{v_{\mathbf{p}}^2 n_{\uparrow}(\mathbf{p} - \hbar k_{\text{r}} \hat{\mathbf{e}}_x) - u_{\mathbf{p}}^2 n_{\downarrow}(\mathbf{p} + \hbar k_{\text{r}} \hat{\mathbf{e}}_x)}{v_{\mathbf{p}}^2 - u_{\mathbf{p}}^2} \quad (4)$$

In Fig. 3(c1-c5), we plot the quasi-momentum distribution in the helicity bases for different atoms density. At the lowest density, the $s = 1$ helicity branch is nearly unoccupied, which is consistent with that the Fermi surface is below $s = 1$ helicity branch. The quasi-momentum distribution of the $s = -1$ helicity branch exhibits clearly a double-peak structure, which reveals the emergence of two disjointed Fermi surfaces at $s = -1$ helicity branch. As density increases, the double-peak feature gradually disappears, indicating the Fermi surface of $s = -1$ helicity branch finally becomes a single elongated one, as the top one in Fig. 3(b). Here we define a quality of visibility $v = (n_{\text{A}} - n_{\text{B}})/(n_{\text{A}} + n_{\text{B}})$, where n_{A} is the density of $s = -1$ branch at the peak and n_{B} is the density at the dip between two peaks. Theoretically one expects v approaches unity at low density regime and approaches zero at high density regime. In Fig 3(d) we show that our data decreases as density increases and agrees very well with a theoretical curve with fixed temperature $T/T_{\text{F}} = 0.65$. Moreover, across the phase boundary between SFS and DFS-1, there will be a significant increase of population on $s = 1$ helicity branch. In Fig. 3 (e), the fraction of atom number population at $s = 1$ helicity branch is plotted as a function of Fermi momentum k_{F} , which grows up rapidly nearby the critical point predicted in zero-temperature phase diagram. The blue solid line is a theoretical calculation for N_{+}/N with $T/T_{\text{F}} = 0.65$, and the small deviation between the data and this line is due to the temperature variation between different measurements. Both two features are consistent with a Lifshitz transition. Recently, topological change of Fermi surface and Lifshitz transition have also been studied in Fermi gas in honeycomb optical lattices, where single particle spectrum exhibits Dirac point behavior [18]. A more

accurate experimental determination of Lifshitz transition point requires more well control of temperature in presence of Raman lasers and the information of local equation-of-state. In the near future, we also plan to bring the system close to a Feshbach resonance where the s -wave interaction becomes strongly attractive, and we will further cool the system below the superfluid transition temperature. There we expect to find Majorana fermion modes at the phase boundaries when Fermi surface topology changes [19–21].

In summary, we have for the first time studied effects of spin-orbit coupling in a ultracold atomic Fermi gas. We study Raman induced spin dynamics and reveal clearly the physical process of spin dephasing due to SO coupling. We measure the momentum distribution in the equilibrium state and find the momentum distribution asymmetry due to the broken of the reflection symmetry caused by SO coupling. We also find evidences for the change of Fermi surface topology and Lifshitz transition from the quasi-momentum distribution in the helicity bases. All these features are unique manifestations of SO coupling in fermionic system, which are absent in previously realized SO coupled boson condensate [1]. This research opens up an avenue toward rich physics of SO coupled Fermi gases.

Methods.

Experimental setup. The experimental setup (see Fig. 1) is the same as discussed in [22–24], which employs a mixture of ^{87}Rb and ^{40}K atoms. In short, a mixture of 1×10^7 ^{87}Rb atoms at the spin state $|F = 2, m_F = 2\rangle$ and 4×10^6 ^{40}K atoms at $|F = 9/2, m_F = 9/2\rangle$ are precooled to $1.5 \mu\text{K}$ by radio-frequency evaporative cooling in a quadrupole-Ioffe configuration (QUIC) trap, and then are transported to the center of the glass cell [25] in favor of optical access. Both species are loaded into the optical dipole trap and further evaporatively cooled in the optical dipole trap by evaporative cooling. At the end of above process, the 2×10^6 ^{40}K atoms reaches quantum degeneracy at $\sim 0.3T_{\text{F}}$. We use a resonant laser beam for 0.03 ms to remove the Rb atoms without heating ^{40}K atoms.

Two laser beams for generating Raman coupling are extracted from a Ti-sapphire laser operating at the wavelength of 773 nm with the narrow linewidth single-frequency and focused at the position of the atomic clouds with $1/e^2$ radii of 200 μm . Two Raman beams are frequency-shifted with -100 MHz and -110.4 MHz by two single-pass acousto-optic modulators (AOM) respectively, and then are coupled into two polarization maintaining single-mode fibers in order to increase stability of the beam pointing and obtain better beam-profile quality. The frequency difference ω of two signal generators for two AOMs is phase-locked by a source locking CW microwave frequency counters. To enhance the intensity stability of the two Raman beams, a small fraction of the light is sent into a photodiode and the regulator is

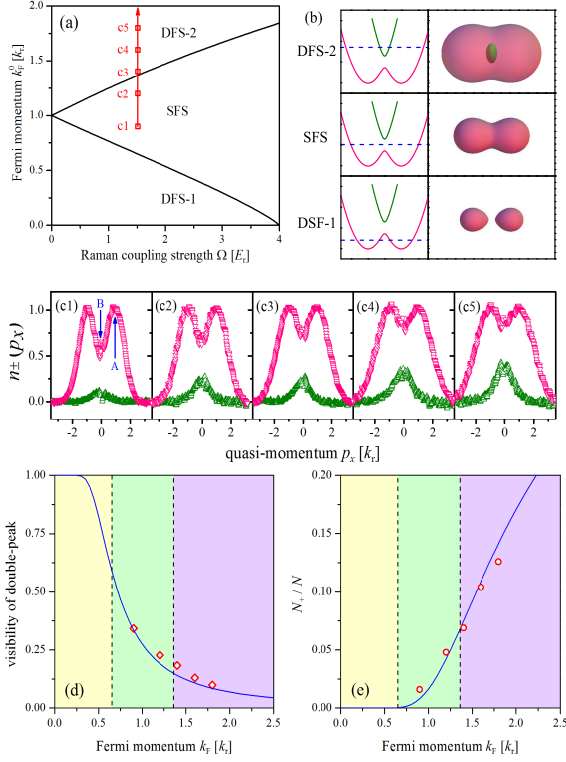


FIG. 3: Topological change of Fermi surface and Lifshitz transition: (a) Theoretical phase diagram at $T = 0$. $k_F^0 = \hbar(3\pi^2 n)^{1/3}$. “SFS” means single Fermi surface. “DFS” means double Fermi surface. (b) Illustration of different topology of Fermi surfaces as Fermi energy increases. The single particle energy dispersion is drawn for small Ω , in which red and green lines are for $s = -1$ and $s = 1$ helicity branches, respectively. Dashed blue line is the chemical potential. Red and green surfaces are Fermi surfaces for $s = -1$ helicity branch and $s = 1$ helicity branch, respectively. (c) Quasi-momentum distribution in the helicity bases. Red and green points are distributions for $s = -1$ and $s = 1$ helicity branches, respectively. $k_F = 0.9k_r$, $T/T_F = 0.80$ for (c1); $k_F = 1.2k_r$, $T/T_F = 0.69$ for (c2); $k_F = 1.4k_r$, $T/T_F = 0.61$ for (c3); $k_F = 1.6k_r$, $T/T_F = 0.63$ for (c4); $k_F = 1.8k_r$, $T/T_F = 0.57$ for (c5). All these points are marked on phase diagram in (a). (d) Visibility $v = (n_A - n_B)/(n_A + n_B)$ decreases as k_F/k_r increases (A and B points are marked in (c1)). (e) Atom number population in $s = 1$ helicity branch N_+/N increases as k_F/k_r increases. In both (d) and (e), the blue solid line is a theoretical curve with $T/T_F = 0.65$, and the background color indicates three different phases in the phase diagram.

used for comparing the intensity measured by the photodiode to a set voltage value from the computer. The non-zero error signal is compensated by adjusting the radio-frequency power in the AOM in front of the optical fiber.

Calculating Momentum Distribution in a Trap. The energy eigenstates for the single particle Hamiltonian in Eq. (1) are the dressed states usually denoted as helicity bases with $s = \pm 1$, with $|+, \mathbf{p}\rangle = u_{\mathbf{p}}|\uparrow, \mathbf{p}\rangle + v_{\mathbf{p}}|\downarrow, \mathbf{p}\rangle$

and $|-, \mathbf{p}\rangle = v_{\mathbf{p}}|\uparrow, \mathbf{p}\rangle - u_{\mathbf{p}}|\downarrow, \mathbf{p}\rangle$, where the coefficients $u_{\mathbf{p}}^2 = 1 - v_{\mathbf{p}}^2 = \frac{1}{2} \left[1 + \frac{p_x v_r - \delta/2}{\sqrt{(p_x v_r - \delta/2)^2 + \Omega^2/4}} \right]$ are only functions of p_x with $v_r = k_r/m$. The energy dispersion for each branch of these dressed states are given by $E_{\pm, \mathbf{p}} = (\mathbf{p}^2 + k_r^2)/(2m) \pm \sqrt{(p_x v_r - \delta/2)^2 + \Omega^2/4}$.

The trapping potential $V(\mathbf{r})$ is taken into account by local density approximation. Even in presence of Raman coupling, what can be measured in the time-of-flight image with Stern-Gerlach technique are still momentum distributions of original hyperfine spin states. Theoretically they are given by

$$n_{\uparrow}(\mathbf{p} - k_r \hat{\mathbf{e}}_x) = \int \frac{d^3 \mathbf{r}}{(2\pi\hbar)^3} \left[u_{\mathbf{p}}^2 f(E_{\mathbf{p},+}; \mathbf{r}) + v_{\mathbf{p}}^2 f(E_{\mathbf{p},-}; \mathbf{r}) \right]$$

$$n_{\downarrow}(\mathbf{p} + k_r \hat{\mathbf{e}}_x) = \int \frac{d^3 \mathbf{r}}{(2\pi\hbar)^3} \left[v_{\mathbf{p}}^2 f(E_{\mathbf{p},+}; \mathbf{r}) + u_{\mathbf{p}}^2 f(E_{\mathbf{p},-}; \mathbf{r}) \right]$$

where $f(E; \mathbf{r})$ is the Fermi-Dirac distribution function with a local chemical potential $\mu(\mathbf{r}) = \mu - V(\mathbf{r})$, and μ is determined by the equation for total particle number

$$N = \int d^3 \mathbf{p} \left[n_{\uparrow}(\mathbf{p}) + n_{\downarrow}(\mathbf{p}) \right] \quad (5)$$

By fitting the measured data to the theoretical curve of integrated momentum profile $n_{1d,\sigma}(p_x) = \int dp_y dp_z n_{\sigma}(\mathbf{p})$ with $\sigma = \uparrow$ or \downarrow , we obtain the temperature of atoms in the experiment.

Interaction Induced Change of Rabi Frequency. We shall also compare this experiment to the clock experiment in Fermi gases [26], where the coupling between two components is momentum independent if the light intensity is assumed to be uniform. In that case, all atoms undergo Rabi oscillation with exact same frequency, and therefore remain as identical particles during the process. Hence, the s -wave interaction plays no role except when the spatial inhomogeneity is taken into account [26]. In contrast, in our case different atoms oscillate with different frequencies, thus they immediately become distinguishable particles as the oscillation starts, and can interact with each other via s -wave collisions. Since our experiment is performed in the weakly interacting regime, we include the interaction effect with mean-field theory.

For a non-interacting system, the equation of motion for a spin $\mathbf{S}_{\mathbf{p}}$ with quasi-momentum \mathbf{p} is given by

$$\frac{\partial}{\partial t} \mathbf{S}_{\mathbf{p}} = \mathbf{S}_{\mathbf{p}} \times \mathbf{h}_{\mathbf{p}} \quad (6)$$

where $\mathbf{h}_{\mathbf{p}} = (-\Omega, 0, k_r p_x/m + \delta)$ is the momentum dependent “effective magnetic field”. The frequency of the spin rotation is given by $|\mathbf{h}_{\mathbf{p}}| = \sqrt{(p_x k_r/m + \delta)^2 + \Omega^2}$, and for $\delta = -4E_r$, it is just the frequency of population oscillation as shown in Eq. (2). For a weakly-interacting system, the interaction can be approximated by $H_{\text{int}} = \frac{g}{V} \mathbf{S} \cdot \mathbf{S}$ at mean-field level, where $g = 4\pi\hbar^2 a_s/m$ is the coupling constant, a_s is the s -wave scattering

length, and $\mathbf{S} = \sum_{\mathbf{p}} \mathbf{S}_{\mathbf{p}}$ is the total spin. Thus, an additional mean-field term appears in the equation of motion,

$$\frac{\partial}{\partial t} \mathbf{S}_{\mathbf{p}} = \mathbf{S}_{\mathbf{p}} \times (\mathbf{h}_{\mathbf{p}} + 2\frac{g}{V}\mathbf{S}). \quad (7)$$

where the solution of $\mathbf{S}_{\mathbf{p}}$ must be determined self-consistently. We numerically solve this equation of motion to determine the spin dynamics. Using the experimental parameters, we find the frequency shift is only a few percent of Ω , which is beyond the measurement resolution of current experiment.

Acknowledgements. We would like to thank Zhenhua Yu, Cheng Chin, Tin-Lun Ho and Sandy Fetter for helpful discussions. This research is supported by National Basic Research Program of China (Grant No. 2011CB921601, 2010CB923103, 2011CB921500), NSFC (Grant No. 10725416, 61121064, 11004118, 11174176), DPFMEC (Approval No. 20111401130001) and Tsinghua University Initiative Scientific Research Program.

[‡] Electronic address: hzhai@mail.tsinghua.edu.cn

[§] Electronic address: jzhang74@sxu.edu.cn; jzhang74@yahoo.com

- [1] Lin, Y.-J., Jiménez-García, K., & Spielman, I. B. Spin-orbit-coupled Bose-Einstein condensates. *Nature* **471**, 83 (2011).
- [2] Wang, C., Gao, C., Jian, C.-M., & Zhai, H. Spin-orbit coupled spinor Bose-Einstein condensates. *Phys. Rev. Lett.* **105**, 160403 (2010).
- [3] Ho, T.-L. & Zhang, S. Bose-einstein condensates with spin-orbit interaction. *Phys. Rev. Lett.* **107**, 150403 (2011).
- [4] For a review, see Hasan, M. Z. & Kane, C. L. Colloquium: Topological insulators. *Rev. Mod. Phys.* **82**, 3045 (2010).
- [5] For a review, see also Qi, X. L. & Zhang, S. C. Topological insulators and superconductors. *Rev. Mod. Phys.* **83**, 1057 (2011).
- [6] Vyasankere, J. P. & Shenoy, V. B. Bound state of two spin-1/2 fermions in a synthetic non-Abelian gauge field. *Phys. Rev. B* **83**, 094515 (2011).
- [7] Vyasankere, J. P., Zhang, S., & Shenoy, V. B. BCS-BEC crossover induced by a synthetic non-Abelian gauge field. *Phys. Rev. B* **84**, 014512 (2011).
- [8] Yu, Z.-Q. & Zhai, H. Spin-orbit coupled Fermi gases across a Feshbach resonance. *Phys Rev Lett.* **107**, 195305 (2011).
- [9] Hu, H., Jiang, L., Liu, X.-J., & Pu, H. Probing anisotropic superfluidity in atomic Fermi gases with Rashba spin-orbit coupling. *Phys. Rev. Lett.* **107**, 195304 (2011).
- [10] Gong, M., Tewari, S., & Zhang, C. BCS-BEC crossover and topological phase transition in 3D spin-orbit coupled degenerate Fermi gases. *Phys. Rev. Lett.* **107**, 195303 (2011).
- [11] Goldman, N., Satija, I., Nikolic, P., Bermudez, A., Martin-Delgado, M. A., Lewenstein, M., & Spielman, I. B. Realistic time-reversal invariant topological insulators with neutral atoms. *Phys. Rev. Lett.* **105**, 255302 (2010).
- [12] Zhai, H. Spin-orbit coupled quantum gases. *Int. J. Mod. Phys. B* **26**, 1230001 (2012)
- [13] Fu, Z., Wang, P., Chai, S., Huang, L., & Zhang, J. Bose-Einstein condensate in a light-induced vector gauge potential using the 1064 nm optical dipole trap lasers. *Phys. Rev. A* **84**, 043609 (2011).
- [14] Lin, Y.-J., Compton, R. L., Perry, A. R., Phillips, W. D., Porto, J. V., & Spielman, I. B. Bose-Einstein condensate in a uniform light-induced vector potential. *Phys. Rev. Lett.* **102**, 130401 (2009).
- [15] Wu, M. W., Jiang, J. H., & Weng, M. Q. Spin dynamics in semiconductors. *Phys. Rep.* **493**, 61 (2010).
- [16] Here, we define Fermi energy and Fermi temperature in the conventional way as the trapped Fermi gas without SO coupling, $E_F = k_B T_F = k_F^2/(2m)$, with $k_F = (24N)^{1/6} \sqrt{\hbar m \omega_{\text{ho}}}$ the Fermi momentum and ω_{ho} the average trap frequency.
- [17] Lifshitz, I. M. Anomalies of electron characteristics of a metal in the high pressure region. *Sov. Phys. JETP* **11**, 1130 (1960).
- [18] Tarruell, L., Greif, D., Uehlinger, T., Jotzu, G., & Esslinger, T. Creating, moving and merging Dirac points with a Fermi gas in a tunable honeycomb lattice. arXiv: 1111.5020, accepted by Nature.
- [19] Lutchnyn, R. M., Sau, J. D., & Das Sarma, S. Majorana Fermions and a topological phase transition in semiconductor-superconductor heterostructures. *Phys. Rev. Lett.* **105**, 077001 (2010).
- [20] Oreg, Y., Refael, G., & von Oppen, F. Helical liquids and Majorana bound states in quantum wires. *Phys. Rev. Lett.* **105**, 177002 (2010).
- [21] Jiang, L., Kitagawa, T., Alicea, J., Akhmerov, A. R., Pekker, D., Refael, G., Cirac, J. I., Demler, E., Lukin, M. D., & Zoller, P. Majorana Fermions in equilibrium and in driven cold-atom quantum wires. *Phys. Rev. Lett.* **106**, 220402 (2011).
- [22] Wei, D., Xiong, D., Chen, H., Wang, P., Guo, L., & Zhang, J. Simultaneous magneto-optical trapping of fermionic ^{40}K and bosonic ^{87}Rb atoms. *Chin. Phys. Lett.* **24**, 1541 (2007).
- [23] Xiong, D., Chen, H., Wang, P., Yu, X., Gao, F., & Zhang, J. Quantum degenerate Fermi-Bose mixtures of ^{40}K and ^{87}Rb atoms in a quadrupole-Ioffe configuration trap. *Chin. Phys. Lett.* **25**, 843 (2008).
- [24] Wang, P., Deng, L., Hagle, E. W., Fu, Z., Chai, S., & Zhang, J. Observation of collective atomic recoil motion in a degenerate Fermion gas. *Phys. Rev. Lett.* **106**, 210401 (2011).
- [25] Xiong, D., Wang, P., Fu, Z., & Zhang, J. Transport of Bose-Einstein condensate in QUIC trap and separation of trapping spin states. *Opt. Express.* **18**, 1649 (2010).
- [26] Campbell, G. K., Boyd, M. M., Thomsen, J. W., Martin, M. J., Blatt, S., Swallows, M., Nicholson, T. L., Fortier, T., Oates, C. W., Diddams, S. A., Lemke, N. D., Naidon, P., Julienne, P., Ye, J., & Ludlow, A. D. Probing interactions between ultracold fermions. *Science* **324**, 360 (2009).